Determination of the spin dynamics in $U_xY_{1-x}Pd_3$ using inelastic neutron scattering

M. J. Bull and K. A. McEwen
Department of Physics and Astronomy, University College London, Gower Street, London WC1E 6BT, United Kingdom

R. S. Eccleston
ISIS Facility, Rutherford Appleton Laboratory, Chilton, Didcot OX11 0QX, United Kingdom

(Received 28 July 1997)

The crystalline electric-field (CEF) excitations in the series of $U_xY_{1-x}Pd_3$ pseudobinary compounds with $x=0.45,0.37,0.28,0.20$ have been measured using inelastic neutron scattering. Two excitations are found in each compound at energy transfers ~ 37 meV and ~ 3 meV that are increasingly hybridized as the uranium concentration is reduced. For $U_{0.45}Y_{0.55}Pd_3$ and $U_{0.37}Y_{0.63}Pd_3$, the low-energy excitation exhibits strong dispersion that is described by a singlet-singlet model of CEF excitations. The CEF parameters are determined for each compound from a comparison of calculated CEF spectra, from which the ground state of $U_{0.45}Y_{0.55}Pd_3$ is deduced to be the nonmagnetic Γ_3 doublet. With decreasing uranium concentration, the low-energy excitation moves towards zero energy transfer, leading to a ground state for $U_{0.2}Y_{0.8}Pd_3$ in which the Γ_3 doublet and Γ_5 triplet states become degenerate. The effect of hybridization and the CEF-level scheme upon the non-Fermi-liquid characteristics of $U_{0.2}Y_{0.8}Pd_3$ are discussed. [S0163-1829(98)00207-0]

I. INTRODUCTION

It is increasingly being discovered that many metallic materials containing *d* or *f* electrons have normal-state properties at variance with the expected behavior predicted from Fermi liquid theory. This is particularly the case for members of the pseudobinary actinide compounds $U_xY_{1-x}Pd_3$ near $U_{0.2}Y_{0.8}Pd_3$, which have been extensively investigated during the past few years.[1–3] This effort has established that the phase diagram of the series comprises materials with long-range magnetic order, spin-glass-type characteristics or non-Fermi-liquid behavior. However, despite the large numbers of bulk property measurements that have helped to characterize the system rather well, microscopic measurements such as neutron scattering remain surprisingly few considering the extent of the information that they can provide.

Neutron scattering measurements of polycrystalline $U_{0.2}Y_{0.8}Pd_3$ were first attempted by Mook *et al.*[4] who identified two low-energy magnetic excitations at energy transfers of ~ 5 meV and ~ 16 meV using a triple-axis spectrometer. However, subsequent experiments by us utilizing the considerable flux and solid angle of detectors available with a chopper spectrometer at a spallation neutron source indicated that the magnetic scattering in the $U_xY_{1-x}Pd_3$ materials extended up to energy transfers of 60 meV, with clear evidence of a peak in the magnetic scattering in the region of 40 meV. Through comparisons with nonmagnetic reference materials it was also shown that the 16 meV peak was in fact related to the phonon density of states, whereas the 5 meV mode was indeed of magnetic origin.[5] Further experiments by Dai *et al.*[6] on polycrystalline $U_{0.45}Y_{0.55}Pd_3$ and $U_{0.2}Y_{0.8}Pd_3$ using polarized neutron scattering produced results in agreement with our data, while also illustrating the difficulty in measuring weak inelastic magnetic signals using triple-axis spectrometers. Additionally, Dai *et al.* reported the formation of long-range antiferromagnetic order in polycrystalline $U_{0.45}Y_{0.55}Pd_3$ at $T=20$ K consistent with bulk susceptibility measurements and with a correlation length >400 Å.

In this paper, we present the results of a comprehensive series of measurements made upon several members of the $U_xY_{1-x}Pd_3$ series of compounds that significantly extend the scope of our previous paper.[5] In Sec. II we describe the neutron spectrometer and data analysis methods used to obtain and characterize the experimental data of Sec. III. An interpretation of the results in terms of the possible crystalline electric field (CEF) level schemes is made in Sec. IV, and in doing so, we illustrate the difficulty that occurs when assigning a correct level scheme to systems such as these in which excited CEF levels are located close to the ground state. We also consider how the large hybridization of the localized uranium $5f$ states with the conduction band may lead to the non-Fermi-liquid effects observed in the bulk properties of $U_{0.2}Y_{0.8}Pd_3$.

II. EXPERIMENTAL METHOD

The inelastic neutron scattering measurements reported in this paper have been made with the HET chopper spectrometer at the UK ISIS spallation neutron source. HET is a direct-geometry time-of-flight instrument in which the energy of the neutron beam incident upon the sample is selected by a fast Fermi chopper located between the moderator and sample position and phased to the 50 Hz pulse rate of the proton accelerator. A nimonic alloy chopper before the Fermi chopper serves to reduce the fast neutron background, and the incident beam is collimated to a cross-sectional area of 45 mm×45 mm at the sample position. Neutrons are scattered from the sample into two forward detector banks, one at low scattering angles $\phi=2.6°\rightarrow 7.2°$ at a distance of 4 m from the sample position, and a second bank covering the higher scattering angles $\phi=9.3°\rightarrow 28.7°$ at a distance of 2.5 m from the sample. Two detector banks located at very high

scattering angles ($\phi = 110.4° \rightarrow 138.7°$) are invaluable for the measurement of the phonon density of states. ^{6}Li-doped scintillator glass monitors are located after the moderator, after the Fermi chopper and after the sample position, while all other detectors are 10 atm ^{3}He gas tubes. A parametrization of the spectrometer resolution function is described in the Appendix.

A. Data analysis

The scattering function $S(\boldsymbol{\kappa},\epsilon)$ in absolute units of mb sr^{-1}meV^{-1}fu^{-1} as a function of wavevector transfer, $\boldsymbol{\kappa}$, and energy transfer, ϵ, is obtained from the raw time-of-flight data by normalizing to the incoherent scattering from a flat vanadium slab standard sample for each chosen incident energy, and then to the incident flux using the integral of the incident beam monitor.

One of the difficulties in analyzing inelastic neutron scattering data from polycrystalline magnetic samples lies in successfully separating magnetic scattering from the underlying phonon modes of the crystal lattice. Inaccurate estimation of the phonon spectrum can frequently lead to misleading interpretations of the magnetic scattering. Two methods are employed here to achieve a successful separation of the two contributions–the ratio method for high incident energies, and a direct method for low incident energies.

The ratio method, first described by Murani,[7] utilizes the fact that any magnetic scattering is reduced to small or zero intensity at high momentum transfers as a result of the wavevector dependence of magnetic form factors. Thus, for the HET spectrometer, the forward scattering banks detect a signal consisting of both magnetic and phonon contributions, whereas at high scattering angles the signal is dominated entirely by the phonon spectrum of the sample. The procedure requires a nonmagnetic polycrystalline reference compound with an identical crystal structure to that of the magnetic compound of interest, and assumes that the phonon scattering in each sample is sufficiently spatially averaged to allow a scaling function to be defined for all energy transfers at any two scattering angles within each sample. The phonon scattering at low angles in the magnetic compound is then obtained by multiplying the high-angle magnetic compound data by the ratio of (low-angle : high-angle) data obtained from the nonmagnetic reference material. The method has the advantage that small shifts in phonon frequencies between the two samples are satisfactorily treated, and was found to be the most reliable way of dealing with phonon spectra estimation in a comparison of methods made by Goremychkin and Osborn.[8]

When using low incident neutron energies, the method fails due to the finite, non-negligible magnitude of magnetic form factors at high scattering angles. In this situation, the only option available is to use the spectra from the reference compound as a direct estimation of the phonon scattering, scaled by the differences in nuclear cross sections between the two samples. Generally, in this situation, the phonon spectra are sufficiently featureless for the frequency shift problems mentioned above to be of no concern.

Data analysis has been carried out using a least squares fitting of spectral functions convoluted with the HET resolution function, detailed balance temperature factor, Debye-Waller factor, and U^{4+} magnetic form factor. This procedure has two stages: (i) the ''background'' phonon spectrum for the scattering angle of interest is obtained from that of YPd_3 and modelled with Lorentzian line shapes, (ii) these ''background'' line shapes are then fixed while suitable additional line shapes are fitted to the magnetic excitations in each spectrum, incorporating the modifying factors pertaining to the magnetic scattering function. We prefer not to subtract the estimated phonon spectrum from the data, since this usually results in large oversubtractions and undersubtractions in the region of the elastic line, making interpretation of the data in this region highly problematic.

B. The CEF neutron scattering function

We briefly summarize here how a calculation of the local static CEF susceptibility can be used to make a comparison with the experimentally determined magnetic neutron scattering function.

The CEF susceptibility, $\chi_{\alpha\alpha}(T)$ obtained using perturbation theory for a magnetic field applied along a crystallographic direction $\alpha = x,y,z$ is written[9]

$$\chi_{\alpha\alpha}(T) = N(g_J\mu_B)^2\Bigg[\beta\sum_i \frac{e^{-\beta E_{\lambda_i}}}{Z}|\langle\lambda_i|J_\alpha|\lambda_i\rangle|^2 + \sum_i\sum_{j\neq i}\frac{1}{Z}\frac{e^{-\beta E_{\lambda_i}}-e^{-\beta E_{\lambda_j}}}{E_{\lambda_j}-E_{\lambda_i}}|\langle\lambda_j|J_\alpha|\lambda_i\rangle|^2\Bigg], \tag{1}$$

where N is the number of magnetic ions, g_J is the Landé g factor, μ_B is the Bohr magneton, $\beta = 1/k_BT$, $|\lambda_i\rangle$ is a CEF eigenfunction with eigenvalue E_{λ_i}, Z is the partition function, J_α is the α component of the total angular momentum of the magnetic ion, and the summations are taken over all allowed eigenstates. The factor of 2 normally found in the Van Vleck term is contained within the summation. If the ground state is nonmagnetic, then the only contribution to the susceptibility at $T=0$ arises from the Van Vleck coupling of the ground state to the excited states, whereas at finite temperatures Curie terms will also be present due to the thermal population of excited states. Within the dipole approximation, the magnetic neutron scattering function can be written in terms of the susceptibility[10]

$$S(\boldsymbol{\kappa},\epsilon) = r_0^2[\tfrac{1}{2}g_JF(\boldsymbol{\kappa})]^2e^{-2W(\boldsymbol{\kappa})}\frac{N}{(g_J\mu_B)^2}\epsilon(1+n(\epsilon)) \times\sum_{\alpha,\beta}(\delta_{\alpha\beta}-\tilde{\kappa}_\alpha\tilde{\kappa}_\beta)\chi'_{\alpha\beta}P_{\alpha\beta}(\epsilon), \tag{2}$$

where $r_0 = -5.4\times10^{-15}$ m, $F(\boldsymbol{\kappa})$ is a single ion magnetic form factor, $e^{-2W(\boldsymbol{\kappa})}$ is the Debye-Waller factor, and $(1+n(\epsilon))$ is the detailed balance factor. $\chi'_{\alpha\beta}$ is the real part of the susceptibility measured at $\boldsymbol{\kappa}=0$ and $\epsilon=0$ and $P_{\alpha\beta}(\epsilon)$ is a relaxation function that integrates to unity. The CEF neutron scattering function is then obtained by combining Eq. (2) with Eq. (1). For polycrystalline samples, the equations must be averaged over all orientations of the scattering vector, and for cubic point group symmetry, $S(\boldsymbol{\kappa},\epsilon)$ can then be written

$$S(\kappa,\epsilon) = \tfrac{1}{2} r_0^2 N (g_J F(\kappa))^2 e^{-2W(\kappa)} \epsilon (1+n(\epsilon)) \times \left[\beta \sum_i p_{\lambda_i} |\langle \lambda_i | J_z | \lambda_i \rangle|^2 \cdot P_i(\epsilon) + \sum_i \sum_{j \neq i} \frac{p_{\lambda_i} - p_{\lambda_j}}{E_{\lambda_j} - E_{\lambda_i}} |\langle \lambda_j | J_z | \lambda_i \rangle|^2 \cdot P_{ij}(\epsilon) \right] = F(\kappa)^2 e^{-2W(\kappa)} \epsilon (1+n(\epsilon)) \sum_\nu A_\nu P_\nu(\epsilon), \quad (3)$$

where we have substituted $p_\lambda = e^{-\beta E_\lambda}/Z$. The excitation spectrum observed by neutron scattering is symmetric about $\epsilon = 0$ at very high temperatures corresponding to upscattering and downscattering events between the populated levels (Van Vleck component), with quasielastic scattering arising from scattering events between the eigenstates of occupied degenerate energy levels (Curie component). At low temperatures this symmetry is strongly affected by the detailed balance factor. Equation (3) can be used to fit experimentally observed CEF excitations, and the contribution of each transition to the bulk susceptibility $\chi'_{\alpha\beta}$ can be determined from the intensities A_ν.

III. EXPERIMENTAL RESULTS

For these experiments, we have examined polycrystalline samples of mass 40–50 g of each of the compounds $U_{0.2}Y_{0.8}Pd_3$, $U_{0.28}Y_{0.72}Pd_3$, $U_{0.37}Y_{0.63}Pd_3$, $U_{0.45}Y_{0.55}Pd_3$, YPd_3 (the nonmagnetic phonon reference material) and $U_{0.2}Th_{0.25}Y_{0.55}Pd_3$. The single phase arc-melted buttons[11] were broken into a number of small fragments to ensure spherically averaged scattering, wrapped in Al foil to give a sample area of 40 mm×40 mm and then aligned and supported so as to be at the beam center within a sealed thin-walled Al slab-shaped sample can containing ^{4}He thermal exchange gas. The sample cans were attached to a closed-cycle refrigerator and cooled to 10 K.

A. Overview of the magnetic scattering

The suitability of YPd_3 as the phonon reference compound for the $U_xY_{1-x}Pd_3$ system is illustrated by a comparison of the scattering at high angles with that of $U_{0.45}Y_{0.55}Pd_3$ using neutrons of incident energy $E_i = 60$ meV, Fig. 1(a). Differences between the two data sets are found only in the intensities of the principal features of each spectrum. At low scattering angles, the intensity of the YPd_3 phonon spectrum drops by a factor ~5 and can be represented by four nonmagnetic Lorentzian components, Fig. 1(b). It should be noted that, above ~25 meV, the scattering intensity is weak and featureless. Below this energy transfer, a sharp, resolution-limited feature at 23 meV is preceded by a broad peak centered at 14 meV. The two remaining components describe the elastic line.

The scattering function of $U_{0.45}Y_{0.55}Pd_3$ requires two additional Lorentzian components to describe the magnetic scattering—one at high energy transfer ~37 meV and one at low energy transfer ~3 meV, Fig. 2(a) ($E_i = 60$ meV). In fitting this data set, the linewidths and intensities of these magnetic components have been allowed to vary freely since

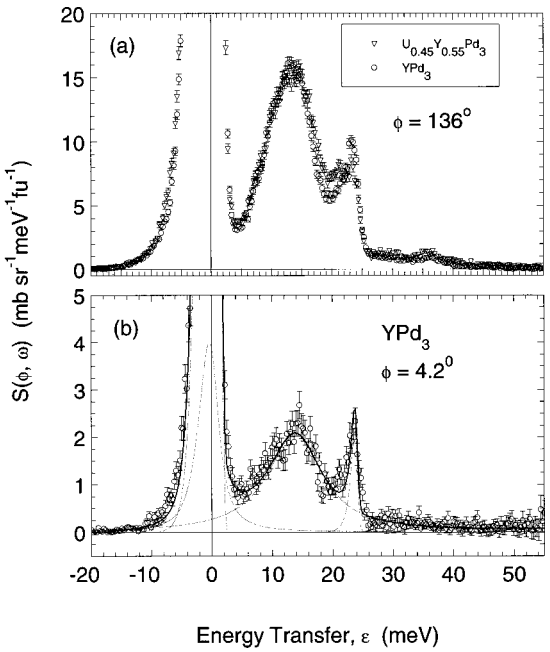

FIG. 1. (a) A comparison of the phonon density of states of $U_{0.45}Y_{0.55}Pd_3$ and the isostructural nonmagnetic reference material YPd_3 at $\phi = 136.3°$ illustrates that YPd_3 is an excellent phonon reference material for the $U_xY_{1-x}Pd_3$ system. (b) The scattering function of YPd_3 at $T = 10$ K is well represented by the sum (solid line) of four Lorentzian line shapes (dashed lines).

constraining the linewidths to be identical produces a highly unsatisfactory fit of the total line shape to the data. The parameters obtained from the fitting process are listed in Table I. As the scattering angle is increased, the excitation intensities are reduced only by the magnetic form factor. At energy transfers close to the elastic line, no magnetic quasielastic component is present and the elastic line is represented entirely by the elastic line components present in the phonon spectrum.

The magnetic scattering from $U_{0.2}Y_{0.8}Pd_3$ with $E_i = 60$ meV is similar to that of $U_{0.45}Y_{0.55}Pd_3$ but with very low excitation intensities and considerably increased linewidths, that can be represented by two Lorentzian line shapes situated at ~36 meV and ~3 meV, Fig. 2(d). However, as a consequence of the results obtained from the low E_i measurements related in the following section, the low-ϵ excitation has been fixed at $\epsilon = 0$, i.e., a *quasielastic* component to the scattering. In fact, the χ^2 statistic of the fitting procedure is only slightly affected by the imposition of this constraint, and the linewidth and intensity of this excitation change only by very small amounts.

Figure 2 also contains data for the intermediate concentration samples, $U_{0.37}Y_{0.63}Pd_3$ and $U_{0.28}Y_{0.72}Pd_3$, and examining the four frames together, it can be seen that there is a *smooth* evolution of the intensities and linewidths of the excitations as the uranium content is reduced. Particularly noticeable is the rapid drop in intensity of the 3 meV excitation. The dashed line in each frame of the figure denotes the scattering from the phonon density of states.

B. Examination of the low energy transfer modes

The low-ϵ region has been examined in greater detail using an incident energy $E_i = 23$ meV, with the associated ben-

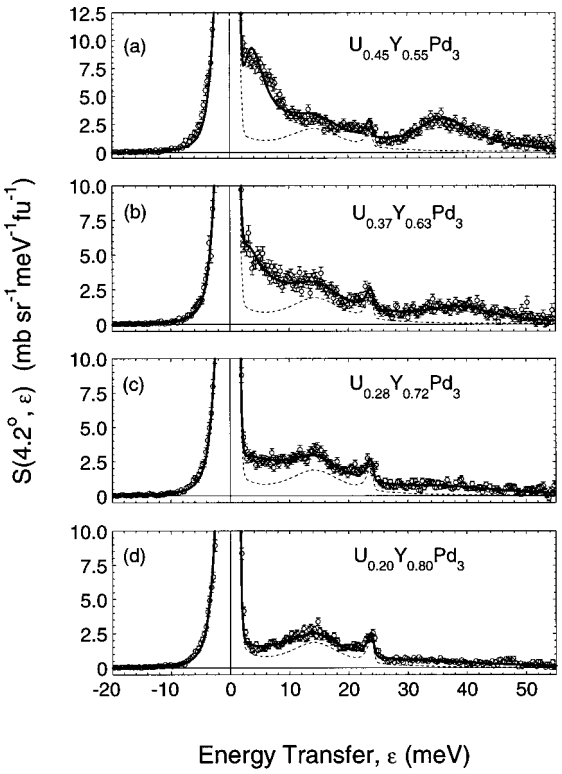

FIG. 2. The evolution of the magnetic scattering in the $U_xY_{1-x}Pd_3$ system at $T=10$ K, $\phi=4.2°$ measured with neutrons of incident energy $E_i=60$ meV. As the uranium concentration is reduced, the two distinct features present in $U_{0.45}Y_{0.55}Pd_3$ decrease in intensity and increase in width, to become very weak for $U_{0.2}Y_{0.8}Pd_3$. The dashed line in each frame indicates the phonon scattering in each compound, and the thick solid line is the result of fitting the data with the sum of the phonon scattering and two magnetic components, one at high energy transfer, ~37 meV, and the other at low energy transfer, ~3 meV.

efits of an almost negligible one-phonon cross section at low scattering angles and multiphonon scattering processes being rare, and clearly demonstrated by the scattering from YPd_3, Fig. 3. The spectrum is simply described by a sharp elastic line with a half-width corresponding to the instrumental resolution of $\Gamma=0.210$ meV convoluted with a slight Lorentzian broadening of half-width $\Gamma=0.055$ meV. For all scattering angles $\phi<30°$, the remaining scattering in each spectrum is described by a sloping linear term. Both the elastic linewidth and the magnitude of the inelastic scattering are independent of scattering angle, and thus allow any additional magnetic scattering to be clearly separated.

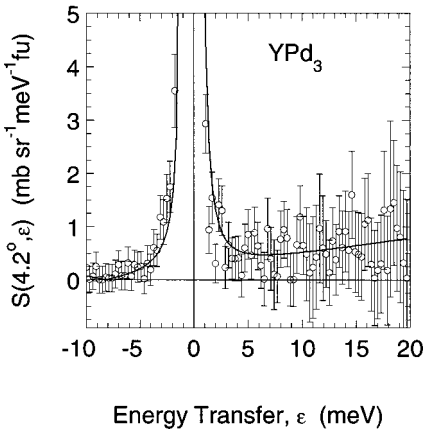

FIG. 3. The inelastic scattering from YPd_3 with an incident energy of 23 meV is featureless and can be represented by an elastic line component and a small linearly increasing background ($\phi=4.2°$).

Four of the spectra obtained from $U_{0.45}Y_{0.55}Pd_3$ at increasing scattering angles are illustrated in Fig. 4 with a strong magnetic excitation present in the region of 3–4 meV, that is initially well separated from the elastic line, and consistent with the excitation observed with $E_i=60$ meV. As ϕ is increased, the excitation exhibits a dispersive nature, moving towards the elastic line before reemerging to again become well separated at $\phi\sim27°$.

The excitation has a Gaussian line shape whose width has been determined from the well-separated peak at 4.2°. Thereafter, data sets at higher scattering angles are fitted with only the intensity and position allowed to vary. The elastic line and sloping inelastic background are kept identical to that of YPd_3 with a slight adjustment (~1–2%) of the elastic line intensity for each spectrum. There is no evidence of any need to include a magnetic quasielastic scattering component.

The dispersion relation obtained from this data, plotted in Fig. 5, reaches a minimum near the Brillouin zone boundary, $\kappa=0.77$ Å^{-1}, indicating the presence of antiferromagnetic correlations between uranium ions. Likewise, the excitation

TABLE I. Energy transfer ϵ, intensity A, HWHM Γ, and wave-vector transfer κ, of the two inelastic Lorentzian components describing the magnetic scattering in the $U_xY_{1-x}Pd_3$ pseudobinary compounds, measured with $E_i=60$ meV at $\phi=4.2°$ and $T=10$ K. The HWHM is excluded for the low-ϵ excitation since more accurate data is available from the $E_i=23$ meV measurements (Table II).

	$U_{0.45}Y_{0.55}Pd_3$	$U_{0.37}Y_{0.63}Pd_3$	$U_{0.28}Y_{0.72}Pd_3$	$U_{0.2}Y_{0.8}Pd_3$
ϵ (meV)	3.0±0.2	1.3±0.3	0.6±0.2	0 Fixed
A (mb sr^{-1}fu^{-1})	19.0±1.0	18.8±1.9	11.8±0.4	5.6±0.3
κ (Å^{-1})	0.4	0.4	0.4	0.4
ϵ (meV)	37.2±0.3	39.3±0.5	37.9±1.4	35.8±1.3
A (mb sr^{-1}fu^{-1})	1.8±0.1	0.9±0.1	0.4±0.1	0.2±0.1
Γ (meV)	5.8±0.5	6.7±0.9	8.5±1.0	10.4±1.5
κ (Å^{-1})	2.1	2.2	2.1	2.0

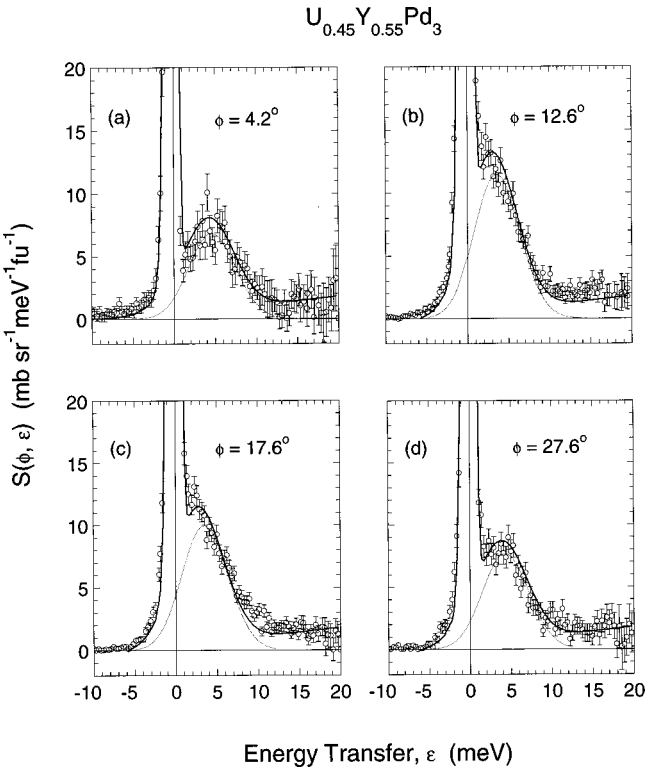

FIG. 4. The low-ϵ dispersive excitation in $U_{0.45}Y_{0.55}Pd_3$ at increasing scattering angles, measured with $E_i = 23$ meV. The initially well-separated Gaussian peak moves into the elastic line before reemerging at higher scattering angles.

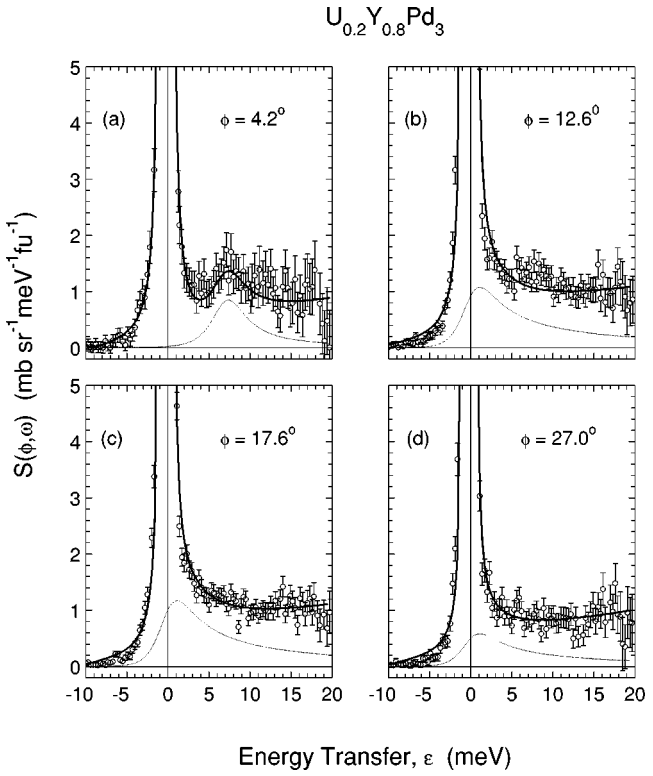

FIG. 6. The inelastic scattering from $U_{0.2}Y_{0.8}Pd_3$ as a function of scattering angle measured with $E_i = 23$ meV. The dispersive feature seen in $U_{0.45}Y_{0.55}Pd_3$ is replaced by a weak, almost κ-independent response. At the lowest scattering angle there occurs an excitation at $\epsilon = 6.9$ meV (a).

intensity reaches a maximum near this zone boundary, Fig. 10(d), and varies in anticorrelation with the energy transfer elsewhere. The increased energy transfer of the excitation in the lowest-angle detector bank, $\epsilon = 4.7$ meV, $\kappa \sim 0.4$ Å^{-1}, relative to the values measured at higher scattering angles arises from the polycrystalline averaging of the dispersion relation and is discussed later in the paper.

In contrast, the inelastic spectra of $U_{0.2}Y_{0.8}Pd_3$ are considerably weaker in intensity and poorly described by a Gaussian function. The elongated form of the scattering is now well described by a Lorentzian function. In addition, the fitting procedure is less straightforward without a distinct excitation like that of $U_{0.45}Y_{0.55}Pd_3$, and as a consequence the location of the peak center becomes arbitrary. In Fig. 6, an overview of the scattering is shown at angles identical to those of $U_{0.45}Y_{0.55}Pd_3$ (Fig. 4) from which all dispersive behavior has apparently disappeared. A general fitting method in which the position and intensity of the Lorentzian are permitted to vary while maintaining a fixed linewidth

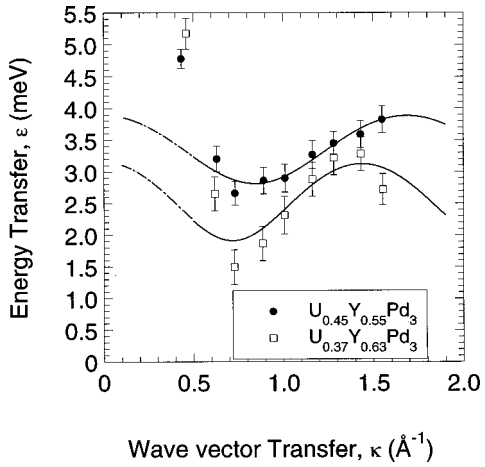

FIG. 5. Dispersion curves derived from the $E_i = 23$ meV data of $U_{0.45}Y_{0.55}Pd_3$ and $U_{0.37}Y_{0.63}Pd_3$. The solid lines are obtained from a singlet-singlet model of crystal-field excitations, Eq. (4).

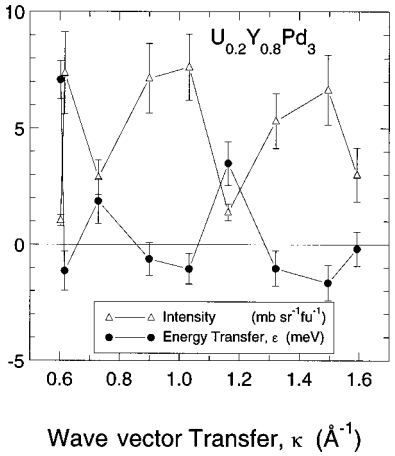

FIG. 7. The variation of the intensity and energy transfer with κ obtained by fitting the $U_{0.2}Y_{0.8}Pd_3$ data of Fig. 6 with a free inelastic Lorentzian function. The intensity and center of this function vary in strict anticorrelation, indicating the presence of intersite exchange interactions.

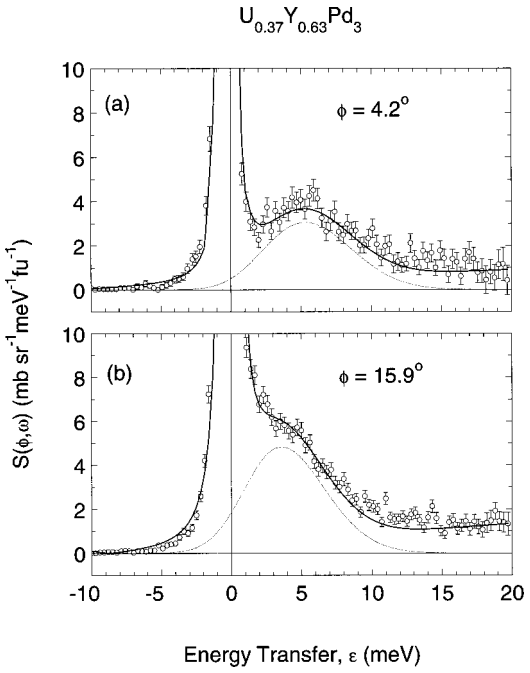

FIG. 8. The low-ϵ excitation in $U_{0.37}Y_{0.63}Pd_3$ is also dispersive with a Gaussian line shape, but occurs at lower-energy transfers than that of $U_{0.45}Y_{0.55}Pd_3$ ($E_i = 23$ meV).

(obtained from the scattering at 4.2°) indicates that the most favored position is one that is close to $\epsilon = 0$ for the higher scattering angles, but with a strictly followed anticorrelation between intensity and energy transfer, Fig. 7, a result indicating that intersite interactions are still present in $U_{0.2}Y_{0.8}Pd_3$. However, it should be noted that, for $\phi = 4.2°$, an inelastic peak is certainly present at $\epsilon = 6.9 \pm 0.7$ meV, Fig. 6(a), which can also be seen (but not fitted successfully) at smaller ϵ in several other spectra.

In another approach, we have fixed the center of the Lorentzian at $\epsilon = 0$ so that any effects of spectral weight shifting that may be present in the above procedure can be eliminated. Despite this constraint, there is still a variation of the Lorentzian intensity with κ, with a maximum in intensity near to the zone boundary, Fig. 10(a), as was found in $U_{0.45}Y_{0.55}Pd_3$. When taken with the anticorrelation of intensity and energy transfer produced by the free Lorentzian function in Fig. 7, it can be concluded that the intersite interactions are still antiferromagnetic.

$U_{0.37}Y_{0.63}Pd_3$, Fig. 8, has a response that is very similar to

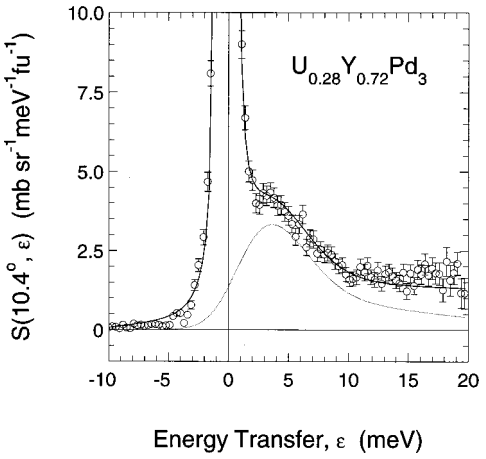

FIG. 9. The line shape of $U_{0.28}Y_{0.72}Pd_3$ ($E_i = 23$ meV) requires a Voigt function (dashed line) to provide a satisfactory fit to the data (solid line).

that of $U_{0.45}Y_{0.55}Pd_3$. The excitation is well fitted by a Gaussian function, with the linewidth again obtained from the well-separated peak in the lowest-angle spectrum at 4.2° and held constant when fitting the remaining spectra. The dispersion curve obtained is plotted in Fig. 5, the intensity variation in Fig. 10(c) and the fit parameters are summarized in Table II.

The spectra of $U_{0.28}Y_{0.72}Pd_3$ are poorly described by both Lorentzian and Gaussian functions, and a satisafctory fit to the data could only be obtained by using a Voigt function in which the half-width at half-maximum (HWHM), Γ, of the Gaussian and Lorentzian components are arranged to be identical. The need for this type of function can be clearly seen in Fig. 9, in which the Gaussian component of the Voigt function matches the ''hump'' close to the elastic line and the Lorentzian component provides the extended tail of scattering. The individual spectra were again fitted with the intensity and peak position allowed to vary, while the linewidth obtained from the low-angle spectrum was held constant. However, the dispersion of the excitation in this case is too small to determine accurately and the excitation position is consequently taken as the mean value, $\epsilon = 1.2 \pm 0.4$ meV. At low scattering angles, the excitation occurs at the much higher energy transfer of $\epsilon = 5.9 \pm 1.1$ meV. The variation of intensity with scattering angle is again more sensitive to the dispersion, reaching a maximum near the zone boundary, Fig. 10(b).

TABLE II. Energy transfer ϵ, intensity A, HWHM Γ, and wave-vector transfer κ, of the magnetic excitation in each compound measured with $E_i = 23$ meV at $T = 10$ K.

		$U_{0.45}Y_{0.55}Pd_3$	$U_{0.37}Y_{0.63}Pd_3$	$U_{0.28}Y_{0.72}Pd_3$	$U_{0.2}Y_{0.8}Pd_3$
Peak type		Gaussian	Gaussian	Voigt	Lorentzian
ϵ (meV)	$\phi = 4.2°$	4.8 ± 0.2	5.2 ± 0.2	5.9 ± 1.1	6.9 ± 0.9
	$\phi > 10°$	3.4 ± 0.2	2.6 ± 0.1	1.2 ± 0.4	0 Fixed
A (mb sr^{-1}fu^{-1})	$\phi = 4.2°$	13.3 ± 1.2	6.7 ± 0.4	8.4 ± 1.1	2.6 ± 0.9
	$\phi > 10°$	20.8 ± 1.3	21.1 ± 2.1	11.1 ± 0.6	7.1 ± 0.7
Γ (meV)	All ϕ	3.7 ± 0.2	4.2 ± 0.3	5.1 ± 0.3	5.6 ± 0.4
κ (Å^{-1})	$\phi = 4.2°$	0.3	0.3	0.4	0.6
	$\phi > 10°$	0.6-1.6	0.6-1.6	0.6-1.6	0.6-1.6

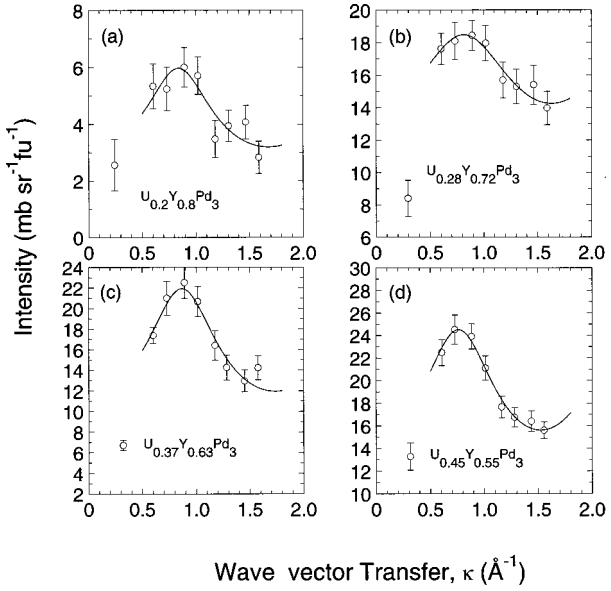

FIG. 10. The intensity variation as a function of κ for the low-ϵ mode in each compound extracted from the $E_i = 23$ meV data sets. The solid lines are obtained using Eq. (5) for the intensity variation within the singlet-singlet model of CEF excitations.

The solid lines plotted through the dispersive data of Fig. 5 and Fig. 10 are the result of fitting the mean field–random-phase approximation equations for the singlet-singlet CEF model.[12] For two singlet states separated by an energy gap Δ, the dispersion relation is written

$$E(\boldsymbol{q}) = [\Delta(\Delta - 2(n_0 - n_1)M^2\mathcal{J}(\boldsymbol{q})]^{1/2}, \qquad (4)$$

where n_0, n_1 are the populations of the ground and excited states, $M = |\langle 1|J_z|0\rangle|$, and $\mathcal{J}(\boldsymbol{q})$ is the $\boldsymbol{q}$-dependent form of the exchange interaction. $\boldsymbol{q}$ is measured from the zone center and in polycrystalline cubic material $\boldsymbol{q}$ is equivalent to $|\boldsymbol{\kappa}|$ within the first Brillouin zone. The form of $\mathcal{J}(\boldsymbol{q})$ is often complex and leads to an antiferromagnetic phase if the maximum value of the exchange occurs at some nonzero value of $\boldsymbol{q}$. However, in this case we have used a simple nearest-neighbor expression for the exchange interaction as a first approximation, $\mathcal{J}(q) = -\mathcal{J}(0)\cos(Cq)$. The neutron scattering intensity also depends upon the dispersion relation,

$$S(\boldsymbol{q},\boldsymbol{\epsilon}) \approx \frac{M^2\Delta}{E(\boldsymbol{q})}[n_0\delta(\boldsymbol{\epsilon} - E(\boldsymbol{q})) + n_1\delta(\boldsymbol{\epsilon} + E(\boldsymbol{q})]. \qquad (5)$$

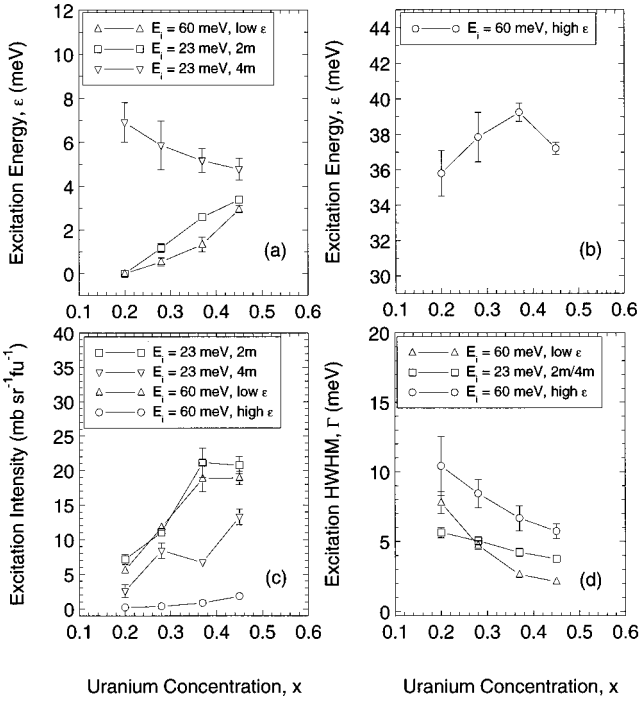

FIG. 11. Overview of the concentration dependence of (a),(b) the excitation energies, (c) intensities and (d) linewidths, for both $E_i = 23$ meV and $E_i = 60$ meV measurements. Values are taken from Tables I and II. Lines connecting points are guides to the eye only.

The values of Δ, $\mathcal{J}(0)$, and C obtained from fitting Eq. (4) and Eq. (5) to the datasets are listed in Table II and Table III.

In Fig. 11 we summarize all of the parameters obtained from the data fitting to enable trends in the parameters to be more clearly visualized. Considering first the excitation energies as a function of uranium concentration, it can be seen that while the position of the high-ϵ excitation [Fig. 11(b)] remains almost constant for each material, the low-ϵ excitation decreases almost linearly with decreasing uranium concentration, Fig. 11(a). This latter frame also indicates that for the $E_i = 23$ meV data, the low-ϵ excitation occurs at a higher-energy transfer at the lowest scattering angle, $\phi = 4.2°$, than the corresponding data at larger scattering angles for each compound, and that the energy transfer of this excitation increases as the uranium content is decreased. We note that this difference is not an instrumental effect arising from systematic errors between the two forward detector banks. Such a large shift in the energy transfer of an excitation could only arise from errors in the flight path

TABLE III. Values of the exchange constant and periodicity of the exchange function $\mathcal{J}(q) = -\mathcal{J}(0)\cos(Cq)$ derived from the dispersion (ϵ) and intensity (A) of the low-ϵ excitation. Where no value is given the quantity could not be determined.

		$U_{0.45}Y_{0.55}Pd_3$	$U_{0.37}Y_{0.63}Pd_3$	$U_{0.28}Y_{0.72}Pd_3$	$U_{0.2}Y_{0.8}Pd_3$
$\mathcal{J}(0)$ (meV)	ϵ	0.059±0.012	0.069±0.021		
	A	0.044±0.013	0.061±0.018	0.049±0.014	0.068±0.019
C (Å)	ϵ	3.7±0.2	4.3±0.2		
	A	4.1±0.2	3.6±0.2	3.9±0.2	3.7±0.2

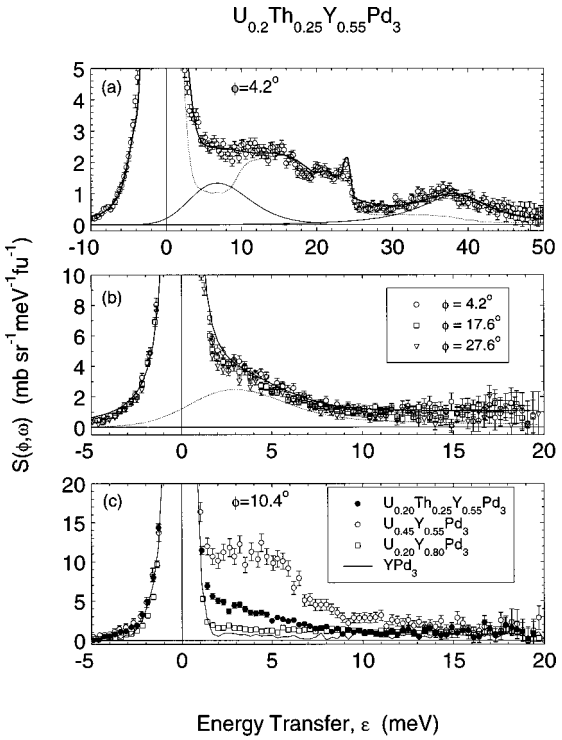

FIG. 12. (a) Doping $U_{0.2}Y_{0.8}Pd_3$ with thorium to form $U_{0.2}Th_{0.25}Y_{0.55}Pd_3$ causes two inelastic peaks to reappear (dashed lines). The thick solid line is the total fit to the data set and the dashed line is the phonon scattering ($E_i = 60$ meV). (b) The low-ϵ magnetic scattering does not exhibit any observable dispersion. A good fit (solid line) to the data set is only obtained through the use of a Voigt function to represent the inelastic peak shape (dashed line). (c) A comparison of the $U_{0.2}Th_{0.25}Y_{0.55}Pd_3$ low-ϵ excitation with those of $U_{0.45}Y_{0.55}Pd_3$ and $U_{0.2}Y_{0.8}Pd_3$ at $\phi = 10.4°$. The signal from YPd_3 is also plotted for comparison.

length calibrations, which are clearly identifiable by a shift of the vanadium incoherent line away from zero energy transfer after conversion of the raw time-of-flight data. This type of error would also result in changes to the energy transfers of the principal excitations in the nonmagnetic reference material YPd_3 between detector banks for both $E_i = 23$ meV and $E_i = 60$ meV data. If the scattering at low angles were to originate from spurious scattering events within the spectrometer, we would expect to find the excitation at the same energy transfer in each sample, and not to exhibit the observed variation with uranium concentration.

The higher energy transfers of the points at lowest scattering angles can be explained by considering the influence that polycrystalline averaging has upon the dispersion relation. For the case of simple nearest-neighbor antiferromagnetic interactions, the exchange interaction has a minimum at the boundaries of the Brillouin zone, and thus the dispersion relation, Eq. (4), will have a periodicity dependent upon the direction of propagation within the zone. The oscillations of the dispersion relation are always centered about the level spacing, Δ, and have an amplitude that is principally controlled by the size of the exchange constant, $\mathcal{J}(0)$. When polycrystalline averaging is introduced, calculations show that the resultant mean dispersion relation is similar to that of Eq. (4), oscillating about the fixed level spacing Δ, but modulated by an additional decaying envelope. The decay envelope is shallower than that indicated by our data, but the required magnitude of damping can be obtained by the inclusion of a next-nearest-neighbor term into the exchange expression such that $\mathcal{J}(q) = -\mathcal{J}(0)\cos(Cq) - \mathcal{J}_2(0)\cos(2Cq)$. The additional term has a doubled periodicity and an independent exchange constant $\mathcal{J}_2(0)$ that can be either antiferromagnetic or ferromagnetic. In this way, it is possible to obtain a decay envelope that mimics the shape of the experimental dispersion curves of Fig. 5 and is still located about Δ. Another important consequence of the averaging is that the apparent exchange integral value $\mathcal{J}(0)$ obtained by fitting Eq. (4) in the κ range of the experiment is dramatically reduced from the value used for the calculation, but that the value of Δ obtained is almost unaffected. Thus, we have only included nearest-neighbor interactions in the exchange integral when fitting the experimental data in order to obtain a value for the level spacing Δ. From an examination of the experimental data of Fig. 5 and Fig. 7, it can be appreciated that the value of Δ is decreasing with decreasing uranium concentration, while the strength of the exchange is increasing, a trend that is also observed in the increasing values of T_K obtained from bulk property measurements.

The excitation intensities, Fig. 11(c), all decrease rapidly as the uranium concentration is reduced, and at a much faster rate than would be expected for a simple scaling by uranium concentration which would estimate the intensity of $U_{0.2}Y_{0.8}Pd_3$ to be $\sim 50\%$ less than that of $U_{0.45}Y_{0.55}Pd_3$, whereas the actual decrease is nearer to 75%. There is a rapid change in the intensity vs concentration plot for the low-ϵ excitation between $x = 0.28$ and $x = 0.37$, a pattern repeated in the susceptibility and resistivity measurements of these samples.[11] The high-ϵ excitation found with $E_i = 60$ meV smoothly decreases in intensity as the uranium concentration is reduced and lies $\sim 90\%$ below that of the low-ϵ excitation. For both excitations, the linewidths increase smoothly with decreasing uranium concentration as the excitations become progressively more damped, Fig. 11(d). The low-ϵ linewidths of $U_{0.45}Y_{0.55}Pd_3$ and $U_{0.37}Y_{0.63}Pd_3$ are underestimated in the $E_i = 60$ meV fitting procedure as a consequence of the initial assumption of a Lorentzian line shape.

TABLE IV. Peak parameters for $U_{0.2}Th_{0.25}Y_{0.55}Pd_3$ at $T = 16$ K.

E_i (meV)		ϵ (meV)	A (mb sr^{-1} fu^{-1})	Γ (meV)	κ (Å^{-1})
60		38.9 ± 1.0 (Lorentzian)	0.8 ± 0.1	6.2 ± 0.8	2.2
		4.1 ± 1.5 (Gaussian)			0.4
23	$\phi = 4.2°$	1.2 ± 0.3 (Voigt)	5.6 ± 1.5	3.4 Fixed	0.3
	$\phi > 10°$	1.2 ± 0.2 (Voigt)	8.4 ± 1.2	3.4 ± 0.6	0.6 - 1.6

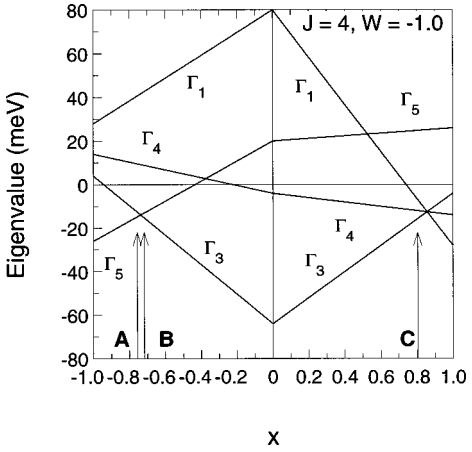

FIG. 13. The Lea, Leask, and Wolf diagram for $J=4$ with $W=-1$. The three positions on the diagram with level spacings matching the experimental results for $U_{0.45}Y_{0.55}Pd_3$ are indicated with arrows.

C. $U_{0.2}Th_{0.25}Y_{0.55}Pd_3$

Doping $U_{0.2}Y_{0.8}Pd_3$ with Th^{4+} ions to create $U_{0.2}Th_{0.25}Y_{0.55}Pd_3$ serves to increase the energy gap between the localized uranium $5f$ states and the Fermi level while simultaneously reducing hybridization with conduction electron states. Thus for $U_{0.2}Th_{0.25}Y_{0.55}Pd_3$, the energy gap is expected to be similar to that of $U_{0.45}Y_{0.55}Pd_3$ while the uranium concentration is identical to that of $U_{0.2}Y_{0.8}Pd_3$. Consequently, the CEF intensities should increase in magnitude from those of $U_{0.2}Y_{0.8}Pd_3$ while the linewidths of the excitations should be reduced.

The results of the $E_i=60$ meV measurement at 16 K are shown in Fig. 12(a) for a scattering angle $\phi=4.2°$. The phonon contribution has again been obtained via the ratio method leaving additional magnetic scattering corresponding to the two CEF excitations observed in the $U_xY_{1-x}Pd_3$ series. The ~ 38 meV transition can be fitted to a Lorentzian line shape, whilst the low-ϵ transition has an irregular shape that fills in the gap in the phonon spectrum around 4 meV. A satisfactory match to this intensity is given by a Gaussian peak shape, but for a quantitative fit, the $E_i=23$ meV data must be used to extract the correct intensity. The parameters obtained are listed in Table IV. Using $E_i=23$ meV to examine the low-ϵ excitation, the best description of the excitation line shape is found to be a Voigt function at all scattering angles. No dispersion could be observed in the data, and the only variation in intensity with scattering angle is produced by the magnetic form factor, Fig. 12(b).

TABLE V. The nine CEF eigenvectors formed from the $J=4$ multiplet in cubic symmetry. $|J_z\rangle \equiv |JLSJ_z\rangle$ are the LS-coupling basis states of the multiplet.

$\|\Gamma_1\rangle$	=	$0.4564\|+4\rangle-0.7638\|0\rangle+0.4564\|-4\rangle$
$\|\Gamma_{3a}\rangle$	=	$0.5401\|+4\rangle-0.6455\|0\rangle+0.5401\|-4\rangle$
$\|\Gamma_{3b}\rangle$	=	$0.7071\|+2\rangle+0.7071\|-2\rangle$
$\|\Gamma_{4a}\rangle$	=	$0.3536\|+3\rangle+0.9354\|-3\rangle$
$\|\Gamma_{4b}\rangle$	=	$0.3536\|-3\rangle+0.9354\|+3\rangle$
$\|\Gamma_{4c}\rangle$	=	$0.7071\|+4\rangle-0.7071\|-4\rangle$
$\|\Gamma_{5a}\rangle$	=	$0.9354\|+3\rangle-0.3536\|-1\rangle$
$\|\Gamma_{5b}\rangle$	=	$0.9354\|-3\rangle-0.3536\|+1\rangle$
$\|\Gamma_{5c}\rangle$	=	$0.7071\|+2\rangle-0.7071\|-2\rangle$

The low-ϵ $U_{0.2}Th_{0.25}Y_{0.55}Pd_3$ peak is compared to those of the $U_xY_{1-x}Pd_3$ series in Fig. 12(c). It can be seen that the $U_{0.2}Th_{0.25}Y_{0.55}Pd_3$ intensity is approximately half that of $U_{0.45}Y_{0.55}Pd_3$, consistent with the difference in uranium content of the two samples, while the linewidth of the excitation is $\sim 20\%$ smaller than that of $U_{0.2}Y_{0.8}Pd_3$, both of which confirm that hybridization effects in $U_{0.2}Th_{0.25}Y_{0.55}Pd_3$ have indeed been reduced.

IV. DISCUSSION AND CONCLUSIONS

A. $U_xY_{1-x}Pd_3$ CEF level scheme

We assume that the uranium ions in the materials considered here have a $5f^2$ electronic configuration based upon the photoemission results of Kang *et al.*[1] and the bulk property measurements of Seaman *et al.*[2] We also note that the CEF excitations in the parent compound UPd_3 strongly support a $5f^2$ electronic configuration.[14] The effect of a cubic CEF upon the $(2J+1)$-degenerate ground-state multiplet of magnetic ions has been considered by Lea, Leask, and Wolf (LLW).[13] For the $J=4$, $5f^2$ configuration, a singlet, a nonmagnetic doublet and two magnetic triplet levels (Table V) are obtained, whose eigenvalues vary with the CEF parameters as shown in the LLW diagram, Fig. 13. Additionally, the transition matrix elements between the nine eigenvectors are listed in Table VI for reference. Note that it has been suggested that structural distortions at low temperature could affect the assumed CEF level scheme. However, our low-temperature high-resolution powder diffraction experi-

TABLE VI. Transition matrix elements $|\langle\Gamma|J_z|\Gamma\rangle|^2$ between the eigenvectors of Table V.

	$\|\Gamma_{3a}\rangle$	$\|\Gamma_{3b}\rangle$	$\|\Gamma_{4a}\rangle$	$\|\Gamma_{4b}\rangle$	$\|\Gamma_{4c}\rangle$	$\|\Gamma_1\rangle$	$\|\Gamma_{5a}\rangle$	$\|\Gamma_{5b}\rangle$	$\|\Gamma_{5c}\rangle$
$\|\Gamma_{3a}\rangle$	0	0	0	0	9.333	0	0	0	0
$\|\Gamma_{3b}\rangle$	0	0	0	0	0	0	0	0	4.00
$\|\Gamma_{4a}\rangle$	0	0	0.250	0	0	0	1.750	0	0
$\|\Gamma_{4b}\rangle$	0	0	0	0.250	0	0	0	1.750	0
$\|\Gamma_{4c}\rangle$	9.333	0	0	0	0	6.667	0	0	0
$\|\Gamma_1\rangle$	0	0	0	0	6.667	0	0	0	0
$\|\Gamma_{5a}\rangle$	0	0	1.750	0	0	0	6.250	0	0
$\|\Gamma_{5b}\rangle$	0	0	0	1.750	0	0	0	6.250	0
$\|\Gamma_{5c}\rangle$	0	4.000	0	0	0	0	0	0	0

ments[11] demonstrate that static distortions do not occur, and thus the point-group symmetry of the uranium ions remains the same between room temperature and 1.6 K.

The CEF parameters for a particular material can be derived from the LLW diagrams, if the experimental excitation energies are known, by searching across a diagram for eigenvalue ratios that match those determined experimentally. This exercise will usually isolate several possible positions for the level scheme on the diagram. To match the overall magnitude of the level scheme to that of the experiment, the computed eigenvalues should then be scaled by the LLW scale parameter W.

Application of this technique to the well-defined excitations of $U_{0.45}Y_{0.55}Pd_3$ produces three possible locations for the CEF parameters of the system on the $J=4$ LLW diagram, indicated by the arrows in Fig. 13, and all lying near crossing points on the diagram. Options A and B, with a negative LLW x parameter, fall on either side of a Γ_5-Γ_3 crossing point, while option C is situated near a Γ_3-Γ_4-Γ_1 crossing point with a positive LLW x parameter. Thus, two level schemes have the non-magnetic Γ_3 doublet as ground state (B and C) while the third has the magnetic Γ_5 triplet as ground state (A).

Having determined the candidate CEF parameters, a means to select the most favorable of these is required. This can be achieved by calculating the intensities (absolute cross sections) of the excitations for comparison with the experimental data. The excitation intensities calculated using Eq. (3) are considerably larger than those measured experimentally, which are reduced due to hybridization processes, and consequently the calculated CEF spectrum must be scaled to match the experimental intensities through the application of a global intensity scale factor. This factor is defined such that the calculated CEF intensity at low-ϵ matches the intensity of the low-ϵ experimental scattering. Scaling first to the calculated intensity of the low-ϵ inelastic peak for each of the schemes A, B, and C yields the curves $A1$, $B1$, and C plotted in Fig. 14(a). The curves are the sum of the experimentally measured phonon scattering plus the *scaled calculated CEF intensity* for the scattering between each of the CEF level groups. The line shapes used are in accord with experiment (Gaussian for the low-ϵ excitation and Lorentzian for that at high ϵ) and are convoluted with the HET resolution function, detailed balance factor and U^{4+} magnetic form factor. It is emphasised that the labeled curves in Fig. 14 *are not fitted* in any way to the data set apart from the application of the global intensity scale factor to the calculated CEF intensity that is listed in Table VII. The global intensity scale factor, distinct from the LLW W parameter that scales the CEF eigenvalues, has a value of 0.297 for $U_{0.45}Y_{0.55}Pd_3$ and is reduced to 0.046 for $U_{0.2}Y_{0.8}Pd_3$. Note also at this point that whichever ground state is finally selected, the observed *trends* in the neutron scattering results remain unaffected and thus instructive.

For curve $A1$ in Fig. 14(a), it is clear that the large Curie term produced by the Γ_5 triplet ground state gives enormous intensity to the quasielastic scattering component, a point further illustrated if this quasielastic intensity is scaled to match the experimental intensity, Curve $A2$, since then the calculated intensity of the high-ϵ excitation is completely suppressed. In contrast, the two schemes with Γ_3 doublet

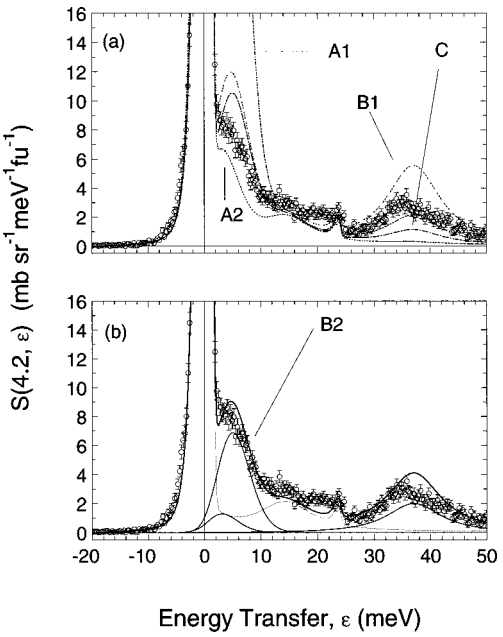

FIG. 14. A comparison of the calculated CEF neutron cross sections with the experimental data of $U_{0.45}Y_{0.55}Pd_3$. The curves are derived from the three candidate level schemes indicated in Fig. 13 and described in more detail in the text. In (b), the thick solid line represents the sum of the measured phonon scattering (dashed line) plus the calculated magnetic components (thin solid lines) of the preferred CEF level scheme. Note that the calculated CEF spectra *have not* been fitted to the data set, other than through the application of a global intensity scale factor.

ground states, curves $B1$ and C, are immediately more representative of the measured scattering. These also have a quasielastic component arising from the thermal population of the low-lying magnetic triplet states, but it is of a considerably smaller magnitude. Curve $B1$ is the most promising choice, with intensities at both low ϵ and high ϵ having the correct ratio, but with just a little too much intensity. However, as a consequence of the detailed balance factor, the intensity arising from the quasielastic component is shifted such that it underlies the intensity from the low-ϵ component, which from the experimental point of view makes the two components indistinguishable since they will appear as one inelastic feature. Thus for level schemes B and C, it is the sum of the quasielastic *and* the low-ϵ inelastic calculated intensities that must be scaled to the experimental result. For scheme C, the scaled intensity by this method is too low to match that of the experiment, whereas there is an extremely good agreement for scheme B, curve $B2$ in Fig. 14(b). The solid lines underneath this curve are the calculated intensities for the transitions within the level scheme, and the dashed line is the experimentally measured phonon scattering. Calculations of the susceptibility, magnetization, and heat capacity for the above level schemes can also be made for comparison with respective bulk property measurements.[11] This comparison further indicates that the magnetic ground state of scheme A is unsuitable—the magnetic heat capacity is underestimated, magnetization curves saturate in very small fields unlike the nearly linear behavior observed, and the susceptibility is too large and Curie like. From these

TABLE VII. CEF parameters for the $U_xY_{1-x}Pd_3$ series of compounds.

x	LLW x	LLW W (meV)	B_{40} (meV)	B_{60} (meV)	Global intensity scale factor
0.45	−0.7175	−1.5427	0.0185	-3.500×10^{-4}	0.297
0.37	−0.7230	−1.6454	0.0198	-3.600×10^{-4}	0.236
0.28	−0.7304	−1.6120	0.0199	-3.430×10^{-4}	0.082
0.20	−0.7370	−1.5452	0.0190	-3.225×10^{-4}	0.046

considerations, level scheme B is taken to be the most representative set of CEF parameters for $U_{0.45}Y_{0.55}Pd_3$:

$$\Gamma_3\ (0.0\ \text{meV}),\ \Gamma_5\ (3.4\ \text{meV}),$$

$$\Gamma_4\ (37.2\ \text{meV}),\ \Gamma_1\ (89.3\ \text{meV}).$$

The quasielastic scattering from the excited Γ_5 triplet level is the most likely source of the weak quasielastic scattering measured by Dai *et al.*[6] at $T=10$ K in polycrystalline $U_{0.45}Y_{0.55}Pd_3$. The CEF parameters for the four $U_xY_{1-x}Pd_3$ samples are listed in Table VII. The experimentally observed movement of the low-ϵ excitation towards $\epsilon=0$ with decreasing uranium concentration is reflected in the CEF parameters which move towards the Γ_3-Γ_5 crossing point. This leads to the following CEF level scheme for $U_{0.2}Y_{0.8}Pd_3$:

$$\Gamma_3\ (0.0\ \text{meV}),\ \Gamma_5\ (0.0\ \text{meV}),$$

$$\Gamma_4\ (35.8\ \text{meV}),\ \Gamma_1\ (85.8\ \text{meV}).$$

All three level schemes allow a singlet-singlet excitation to occur, and so this cannot be used to help isolate the correct level scheme. This can be seen by referring to the transition matrix elements in Table VI. Transitions are permitted between either eigenvector of the Γ_3 doublet and the single nonmagnetic eigenvector contained in each triplet level, and thus explains why the low-ϵ excitation follows a singlet-singlet dispersion relation.

For magnetic order to arise from a nonmagnetic ground state, the exchange interaction must exceed the respective critical value for each level scheme, $\mathcal{J}_{\text{crit}}=\Delta/2M^2$,

$$\text{Scheme B: } \Gamma_3\rightarrow\Gamma_5\ \ \mathcal{J}_{\text{crit}}\sim0.375\ \text{meV},$$

$$\text{Scheme C: } \Gamma_3\rightarrow\Gamma_4\ \ \mathcal{J}_{\text{crit}}\sim0.161\ \text{meV}.$$

As has been discussed earlier, the strength of the exchange interaction obtained from the dispersive data of $U_{0.45}Y_{0.55}Pd_3$ [$\mathcal{J}(0)\sim0.05$ meV], is significantly reduced from the true value as a result of the polycrystalline averaging of the dispersion relation within the sample. Nevertheless, an estimate of the actual exchange constant can be made by considering the immediate nearest-neighbor environment of each uranium ion. Nearest neigbors order antiferromagnetically in the a-b plane but successive planes along the c axis are stacked ferromagnetically.[6,11] Hence, the exchange constant along the c axis, $\mathcal{J}_c$, is opposite in sign and of slightly larger magnitude than the exchange constant in the a-b plane, $\mathcal{J}_a$. For example, if $\mathcal{J}_c=-1.1\mathcal{J}_a$, then the measured exchange constant will be $\mathcal{J}_{\text{exp}}=(4\mathcal{J}_a+2\mathcal{J}_c)/6=0.3\mathcal{J}_a$, which gives a value of $\mathcal{J}_a(0)\sim0.17$ meV for $U_{0.45}Y_{0.55}Pd_3$ and is of the correct order of magnitude to exceed $\mathcal{J}_{\text{crit}}$. Thus, a nonmagnetic ground state in polycrystalline $U_{0.45}Y_{0.55}Pd_3$ does not exclude the formation of long-range magnetic order.

B. Discussion and conclusions

The rapid reduction in the intensity of the CEF excitations, together with the associated increase in the linewidth arising from the hybridization of localized $5f$ states with conduction electron states, can be understood in the context of Fermi-level tuning introduced by Kang *et al.*[1] The substitution of Y^{3+} ions for U^{4+} ions removes electrons from the system, reducing the energy gap between the Fermi level and the local $5f$ CEF levels. The effect is not unique but is particularly noticeable in this system in which the excitation intensities are reduced by $\sim$70–80 % in going from $U_{0.45}Y_{0.55}Pd_3$ to $U_{0.2}Y_{0.8}Pd_3$ (Tables I and II). This reduction is considerably greater than the 55% reduction in intensity expected purely from the difference in uranium content between the two materials. Indeed, a calculation of the relative changes between the scale factors of Table VII, which reflect the increasing hybridization beween the $5f$ and conduction electron states, would be an interesting challenge for condensed matter theorists.

The effect of Fermi level tuning on the bulk properties is noticeable in the crossover in sample response from being CEF dominated at high uranium concentrations ($x>0.35$) to one that is dominated by the conduction electrons at low uranium concentrations.[2,11] This crossover is also reflected here by the change in line shape of the low-ϵ excitation from Gaussian to Lorentzian via the mixed Voigt function occuring for $U_{0.28}Y_{0.72}Pd_3$. However, while the change in linewidth can be related to the hybridization processes, it is unclear how the line shape change from Gaussian to Lorentzian via the intermediate Voigt function should be explained, nor whether this change can be interpreted solely within the concept of Fermi-level tuning.

Similarly, the results from $U_{0.2}Th_{0.25}Y_{0.55}Pd_3$ can be interpreted in terms of Fermi-level tuning. The increased number of conduction electrons provided by the thorium moves the Fermi level away from the local CEF levels reducing the hybridization with the conduction electron states. Uranium ion intersite interactions reappear due to the increased localization of the $5f$ electrons and produce an irreversible transition in the susceptibility data, although the strength of the interactions is too weak to result in any measurable dispersion of the low-ϵ excitation. Thus it can be concluded that the non-Fermi-liquid properties of $U_{0.2}Y_{0.8}Pd_3$ are controlled purely by the critical positioning of the Fermi level and that intersite interactions are only of secondary importance.

The relaxation function of magnetic impurities in metallic systems frequently has a Lorentzian line shape arising from conduction electron scattering, with a HWHM that scales as $\Gamma(T) \propto T$.[15,16] In the presence of Kondo impurities, the relaxation rate saturates below T_K and the line shape has a HWHM $\Gamma(0) \propto T_K$. This is observed in classical Kondo systems such as the AuFe dilute spin glass systems and also in some of the more concentrated Kondo lattice materials. Of course, in these more concentrated systems, above the respective characteristic temperature the linear dependence of Γ is usually modified, with a $T^{1/2}$ dependence in some heavy fermion systems for example. The quasielastic magnetic scattering in $U_{0.2}Y_{0.8}Pd_3$ has a HWHM $\Gamma = 65.4 \pm 4.2$ K, which is of a comparable size to the value of T_K obtained from bulk measurements.[3] We also note that the change in Γ between $U_{0.2}Y_{0.8}Pd_3$ and $U_{0.28}Y_{0.72}Pd_3$ of 16–18 % is of the same size as the change in T_K determined from measurements of $\rho(T)$ on the same materials.[11] This relationship between the low-T Γ value and T_K is identical to that of conventional heavy fermion materials. Thus from the above results, we conclude that the magnetic properties of $U_{0.2}Y_{0.8}Pd_3$ are of a predominantly single-ion nature, a conclusion that has also been reached by Maple *et al.*[3] from macroscopic experimental results. It should be noted that the macroscopic properties of our samples are in excellent agreement with those published by other groups. Elsewhere we report the results of our resistivity, susceptibility, heat capacity, and magnetization measurements for these samples, in addition to the results of our low-temperature neutron powder diffraction and μSR experiments.[11]

In summary, we have measured the CEF excitations in several members of the $U_xY_{1-x}Pd_3$ series of compounds and have been able to assign a CEF level scheme that explains the changes in magnetic properties that occur with decreasing uranium concentration. In making this assignment, we have illustrated that the assignment of a correct level scheme to the higher uranium content samples is a nontrivial task. We have also found that in the samples with higher uranium concentrations, the magnetic intersite interactions responsible for antiferromagnetic order cause the low-ϵ CEF excitation to exhibit dispersive behavior. However, it would appear that these intersite interactions play only a minor role in the formation of the non-Fermi-liquid behavior observed in $U_{0.2}Y_{0.8}Pd_3$.

ACKNOWLEDGMENTS

This work was supported by the UK Engineering and Physical Sciences Research Council. Grateful thanks for the preparation of excellent samples are given to A. R. Bradshaw and D. Fort at the University of Birmingham and to D. Hinks at Argonne National Laboratory.

APPENDIX: HET RESOLUTION FUNCTION

The passage of neutrons through the H_2O moderator and their subsequent journey through the components of the spectrometer sets an intrinsic minimum width in energy and momentum coordinates on any feature measured by the instrument. Knowledge of the instrumental resolution is an important factor when examining excitations with an intrinsic width due to relaxation processes within the sample. The measured experimental width of any excitation is then a convolution of the instrumental resolution with the intrinsic width of the excitation.

A simple parametrization of the HET resolution function has been used in the data analysis here that proves to be an excellent substitute for the full resolution calculation. The resolution function, $\sigma(\epsilon)$ of the instrument can be written in terms of the time widths introduced by the moderator and the chopper opening time,[17]

$$\begin{aligned}\sigma(\epsilon) &= \left\{ \left[2\frac{\Delta t_{\rm chop}}{t_{\rm mc}} \left(1 + \frac{L_{\rm mc}+L_{\rm cs}}{L_{\rm sd}} \left(1 - \frac{\epsilon}{E_i} \right)^{3/2} \right) \right]^2 \right. \\ &\quad \left. + \left[2\frac{\Delta t_{\rm mod}}{t_{\rm mc}} \left(1 + \frac{L_{\rm cs}}{L_{\rm sd}} \left(1 - \frac{\epsilon}{E_i} \right)^{3/2} \right) \right]^2 \right\}^{1/2} \\ &\equiv \left\{ \left[2\frac{\Delta t_{\rm chop}}{t_{\rm mc}} \mathcal{M}(\epsilon) \right]^2 + \left[2\frac{\Delta t_{\rm mod}}{t_{\rm mc}} \mathcal{C}(\epsilon) \right]^2 \right\}^{1/2} \end{aligned} \tag{A1}$$

in which $\Delta t_{\rm chop}$ is the uncertainty in flight time introduced by the chopper, $t_{\rm mc}$ is the flight time from the moderator to the chopper, $L_{\rm mc}$ is the length from moderator to chopper, $L_{\rm cs}$ is the length from chopper to sample and $L_{\rm sd}$ is the length from the sample to the detector. $\epsilon = E_i - E_f$ is the energy transfer between the neutron and sample for neutrons with incident energy E_i and final energy E_f. $\Delta t_{\rm mod}$ is the uncertainty in neutron flight time introduced by the moderator. The experimental resolution of the spectrometer can be obtained by measuring the incoherent scattering from a vanadium sample and has the characteristic line shape of a Gaussian convoluted with a decaying exponential, standard deviation $\sigma_{\rm van}$. It has been shown[18] that there is a good agreement between experiment and calculation for the chopper contribution to the resolution function, $\sigma_{\rm chop}$, and thus the moderator contribution, $\sigma_{\rm mod}$, which is difficult to calculate accurately, can be obtained from $\sigma_{\rm van}$ for a particular E_i,

$$\sigma_{\rm mod} = \sqrt{\sigma_{\rm van}^2 - \sigma_{\rm chop}^2}. \tag{A2}$$

Since the resolution of the spectrometer at the elastic line ($\epsilon = 0$) is measured by $\sigma_{\rm van}$, the value at any finite ϵ can thus be calculated:[19]

$$\sigma_{\rm exp}(\epsilon) = \sqrt{\left(\sigma_{\rm mod} \times \frac{\mathcal{M}(\epsilon)}{\mathcal{M}(0)} \right)^2 + \left(\sigma_{\rm chop} \times \frac{\mathcal{C}(\epsilon)}{\mathcal{C}(0)} \right)^2}. \tag{A3}$$

For example, for the $E_i = 23$ meV measurements in this paper, the resolution decreases from $\sigma = 0.27$ meV at $\epsilon = 0$ meV to $\sigma = 0.11$ meV at $\epsilon = 23$ meV.

[1] J. S. Kang, J. W. Allen, M. B. Maple, M. S. Torikachvili, W. P. Ellis, B. B. Pate, Z. X. Shen, J. J. Yeh, and I. Lindau, Phys. Rev. B **39**, 13 529 (1989).

[2] C. L. Seaman, M. B. Maple, B. W. Lee, S. Ghamaty, M. S. Torikachvili, J. S. Kang, L. Z. Liu, J. W. Allen, and D. L. Cox, Phys. Rev. Lett. **67**, 2882 (1991).

[3] M. B. Maple, R. P. Dickey, J. Herrmann, M. C. de Andrade, E. J. Freeman, D. A. Gajewski, and R. Chau, J. Phys.: Condens. Matter **8**, 9773 (1996).

[4] H. A. Mook, C. L. Seaman, M. B. Maple, M. A. Lopez de la Torre, D. L. Cox, and M. Makivic, Physica B **186-188**, 341 (1993).

[5] K. A. McEwen, M. J. Bull, R. S. Eccleston, D. Hinks, and A. R. Bradshaw, Physica B **206&207**, 112 (1995).

[6] P. Dai, H. A. Mook, C. L. Seaman, M. B. Maple, and J. P. Koster, Phys. Rev. Lett. **75**, 1202 (1995).

[7] A. P. Murani, Phys. Rev. B **28**, 2308 (1983).

[8] E. A. Goremychkin and R. Osborn, Phys. Rev. B **47**, 14 280 (1993).

[9] S. K. Chan and D. J. Lam, in *The Actinides: Electronic Structure and Related Properties*, Vol. 1 (Academic Press, New York, 1974).

[10] S. W. Lovesey, *Theory of Neutron Scattering from Condensed Matter* (Oxford University Press, Oxford, 1984), Vol. 2, p. 43.

[11] M. J. Bull and K. A. McEwen (unpublished); M. J. Bull, Ph.D. thesis, University of London, 1996.

[12] J. Jensen and A. R. Mackintosh, *Rare Earth Magnetism: Structures and Excitations* (Oxford University Press, Oxford, 1991).

[13] K. R. Lea, M. G. M. Leask, and W. P. Wolf, J. Phys. Chem. Solids **23**, 1381 (1962).

[14] A. F. Murray and W. J. L. Buyers, in *CEF and Structural Effects in f-electron Systems* edited by J. E. Crow and R. P. Guertin (Plenum Press, New York, 1980), p. 257; K. A. McEwen U. Steigenberger and J. L. Martinez, Physica B **186-188**, 670 (1993).

[15] J. Korringa, Physica (Amsterdam) **16**, 601 (1950).

[16] M. B. Walker, Phys. Rev. B **1**, 3690 (1970).

[17] C. G. Windsor, *Pulsed Neutron Scattering* (Taylor & Francis Ltd., London, 1981), Chap. 8.

[18] T. G. Perring, Rutherford Appleton Laboratory Report No. RAL 94-025, 1994 (unpublished).

[19] R. Osborn (private communication).